metals

MDPI

Article

The Role of Microstructure on Tensile Plastic Behavior of Ductile Iron GJS 400 Produced through Different Cooling Rates, Part I: Microstructure

Giuliano Angella [1], Dario Ripamonti [1,*], Marcin Górny [2], Stefano Masaggia [3] and Franco Zanardi [3]

1 Institute of Condensed Matter Chemistry and Technologies for Energy (ICMATE), National Research Council of Italy, via R. Cozzi 53, 20125 Milano, Italy; giuliano.angella@cnr.it
2 Faculty of Foundry Engineering, Department of Cast Alloys and Composites Engineering, AGH University of Science and Technology, 30-059 Kraków, Poland; mgorny@agh.edu.pl
3 Zanardi Fonderie S.p.A., via Nazionale 3, 37046 Minerbe (VR), Italy; MST@zanardifonderie.com (S.M.); franco.zanardi@icloud.com (F.Z.)
* Correspondence: dario.ripamonti@cnr.it; Tel.: +39-02-66173-323

Received: 29 August 2019; Accepted: 26 November 2019; Published: 29 November 2019

Abstract: A series of samples made of ductile iron GJS 400 was cast with different cooling rates, and their microstructural features were investigated. Quantitative metallography analyses compliant with ASTM E2567-16a and ASTM E112-13 standards were performed in order to describe graphite nodules and ferritic grains. The occurrence of pearlite was associated to segregations described through Energy Dispersive X-ray Spectroscopy (EDS) analyses. Results were related to cooling rates, which were simulated through MAGMASOFT software. This microstructural characterization, which provides the basis for the description and modeling of the tensile properties of GJS 400 alloy, subject of a second part of this investigation, highlights that higher cooling rates refines microstructural features, such as graphite nodule count and average ferritic grain size.

Keywords: ductile iron; cooling rate; segregation; microstructure

1. Introduction

Ductile Irons (DIs) are ternary Fe-C-Si alloys in which graphite forms as spheroidal particles (nodules), allowing for a good compromise between mechanical properties and a low production cost [1,2]. The number of graphite nodules and their shape are the result of a various technological factors which influence cooling rate and physicochemical state of the liquid metal [1,3,4]. The cooling rate is mainly affected by the wall thickness, the thickness of the neighboring parts of the casting section, and the initial temperature of the metal and mold and the mold material to absorb heat. The physicochemical state of the liquid metal is in turn affected primarily by the chemical composition, charge materials, furnace atmosphere, holding time, liquid metal superheating, preconditioning, spheroidization, and inoculation processes used in the foundry practice [1–11]. The cooling conditions under which the eutectoid reaction takes place together with alloying elements influence the metallic matrix microstructure [12–14]. So, the production route to design and shape optimal ductile iron microstructures with proper mechanical properties is very complex, involving aforementioned different factors, as well as implemented heat treatment conditions [15,16].

Silicon is a graphitizer element which hinders the occurrence of iron carbide. Its effect is estimated via the CE (Carbon Equivalent) relationship, CE = %C + 1/3%Si. A CE value of 4.26 denotes the eutectic composition [1]. Silicon seems to play a negligible role in determining the ferrite grain size, and it can segregate around the graphite nodules, thus being a possible cracking site [17].

Copper is a common alloying element in DI because of its graphitizing effect. It promotes pearlite formation, in particular, when coupled with small Mn additions [18].

The chemical composition together with the cooling conditions after casting affect the microstructure of the alloy. A number of parameters, describing the cooling curve, can be found in literature (a list is provided in [1,2]) that may be related to the graphite shape. In this work, the transformation temperatures and the corresponding undercooling will be taken into account. The inoculation practice and the cooling rate cooperates to control the nodule count, while the conditions under which the eutectoid reaction takes place influence the matrix microstructure [12,13].

The tensile plastic behavior of ductile iron is very sensitive to microstructure and casting defects. In this connection, strain hardening analysis is a powerful tool to study the effect of microstructure on its tensile plastic behavior of ductile iron. Angella et al. [19] shows that the dislocation-density-related Voce equation describes properly the correlations between strain hardening and microstructure of metallic alloys. From published literature [19–24], there is limited information on the effect of microstructure on tensile plastic behavior of ductile iron in terms of the strain hardening effect and micro-mechanisms occurring during deformation of its microstructure. Hence, the tensile flow curves modeling associated with an explicit correlation between plastic behavior and some microstructure parameters have not yet been clearly disclosed. This work, which provides the microstructural basis for the description and modeling of the tensile behavior of GJS 400 alloy [25], will investigate the correlation between the cooling rates near eutectic and eutectoid transformations and the microstructural features of the alloy. Cooling rates are estimated through MAGMAsoft v.5.3 taking into account the solidification of actual samples.

2. Materials and Methods

The chemical composition of the GJS 400 produced by Zanardi Fonderie S.p.A. (Minerbe-VR, Italy) is reported in Table 1. Carbon and sulfur contents were measured through a combustion infrared detection technique with a LECO CS744 by LECO (St. Joseph, MI, USA), while the other elements were detected by optical emission spectrometer with a ARL3460 by Thermo Fisher Scientific (Waltham, MA, USA). The value of CE is 4.45%, which makes the alloy hypereutectic. The residual Mg is 0.046%, which allows for graphite spheroidization [2].

Table 1. Chemical compositions of GJS 400 alloy (wt%).

C	Si	Mn	Cu	Ni	Cr	Mg	P	S	Fe
3.63	2.45	0.129	0.133	0.0168	0.023	0.046	0.038	0.0061	Bal.

Nodularization treatment was performed in a tundish cover ladle, using a Fe–Si–Mg alloy (Si 45 wt%, Mg 6,5 wt%), together with the alloying elements needed to achieve the desired chemical composition. After alloying, the melt was gravity poured in horizontal green sand molds (silica sand with clay and sea–coal addition, plus 3.5% water to activate clay), shaped with a pattern plate and formed with a green sand molding plant, in order to obtain the following samples complying with EN 1563 standard [26], namely (Figure 1):

1. a Lynchburg sample with 25 mm diameter; and
2. three Y-blocks samples with thickness 25, 50, and 75 mm.

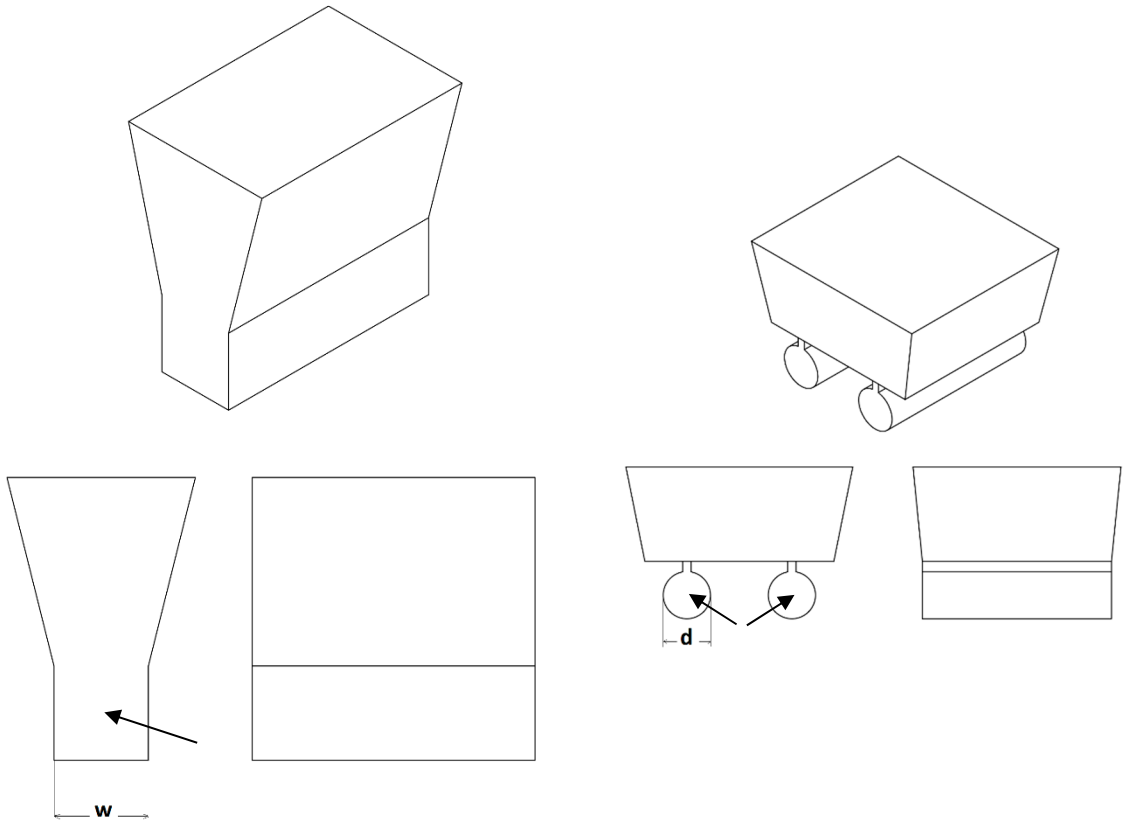

Figure 1. Sketches of the samples used. The upper part "feeds" the lower one, at the barycenter of which specimens were taken (see arrows). (**a**) 3D representation and orthographic projections of Y-block sample, w = 25, 50, 70 mm; (**b**) 3D representation and orthographic projections of Lynchburg sample, d = 25 mm.

The liquid metal was poured into the molds through the pouring basin and then, by mean of the gating system, it filled the cavity of all the samples. Specimen for metallographic analyses were taken in the lower part of the samples (see Figure 1). In particular, six specimens from each samples were investigated through Scanning Electron Microscopy (SEM) with a SU70 microscope by Hitachi (Tokyo, Japan) equipped with Energy Dispersive X-ray Spectroscopy (EDS) detector (Noran 6 system by Thermo Fisher Scientific (Waltham, MA, USA) for elemental microanalysis. The acceleration voltage was 20 kV and the working distance was about 15 mm. After conventional mechanical polishing, the samples were etched with Nital 10% for 5 s to highlight the grain boundaries of the ferritic matrix and the pearlitic islands. Nodule count, nodularity, average diameter of the graphitic nodules, and volumetric fractions of graphite and pearlite were determined through Digital Image Analysis, by means of ImageJ software [27], of SEM images complying with ASTM standard E2567-16a [28], whilst the determination of the average ferritic grain size was carried out through OM complying with ASTM standard E112-13 [29]. ASTM standards were chosen because to the authors' experience they are more commonly used.

ASTM standard E2567-16a requires that at least 500 graphite particles with a minimum MFD (Maximum Feret diameter) of 10 μm must be analyzed. A particle with a shape factor (ratio between the area of the particles and the area of the reference circle, this latter being related to the MFD) higher than 0.60 is defined as a nodule. Nodularity is then defined as the ratio between the total area of the nodules and the total area of the graphite particles. Nodule count is given by the ratio of the nodules and the test area, expressed in mm^2.

Grain size measurement were performed through the Hilliard single-circle procedure described in the ASTM standard E112-13. A single circle was blindly applied on at least five fields. A minimum of 35 intercepts between the circle and the grain boundaries is required. The ASTM grains size G is calculated as a function of the mean intercept, i.e., the ratio of the test line and the number of intercept. The average grain size can be thus calculated.

Since no direct measurement was possible, simulations of temperatures during cooling were performed through the Iron Module of the commercial software MAGMASOFT v5.3 by MAGMA (Aachen, Germany) in order to correlate cooling conditions with the microstructure. The inputs for this simulation are the 3D geometry of the casting system, the chemical composition of the alloy, the thermophysical parameters of the materials involved and alloy-mold and mold-environment heat transfer coefficients. The thermophysical parameters of the green sand, in particular the thermal conductivity, used for the simulation were determined by Zanardi Fonderie S.p.A. through an extensive experimental campaign aimed at the fine tuning of the parameters governing the heat fluxes. The actual set up of the gravity casting process was taken into account.

3. Results

3.1. Simulated Cooling Curves

The molten metal experienced significantly different solidification rates. Simulations of the casting system consisting of molten metal poured into sand molds were performed in Zanardi Fonderie S.p.A., and the cooling curves are reported in Figure 2. Data refer to the barycenter of the lower portion of the samples, where the specimens for metallographic analyses were taken. Eutectic (T_s) and eutectoid (T_e) equilibrium temperatures can be estimated on the basis of the chemical composition [14,30]:

$$T_s = 1154°C + 5.25\%Si - 14.88\%P = 1166.3\ °C; \quad (1)$$

$$T_e = 739°C + 18.4\%Si + 2\%Si^2 - 14\%Cu - 45\%Mn + 2\%Mo - 24\%Cr - 27.5\%Ni + 7.1\%Sb = 787.8,\ °C \quad (2)$$

where "%el" represents the weight content of the element in the alloy. These equations hold for Si content up to 3 wt%, Mn, Cu, Cr, Ni content up to 1 wt%, and Mo content up to 0.5 wt% [14].

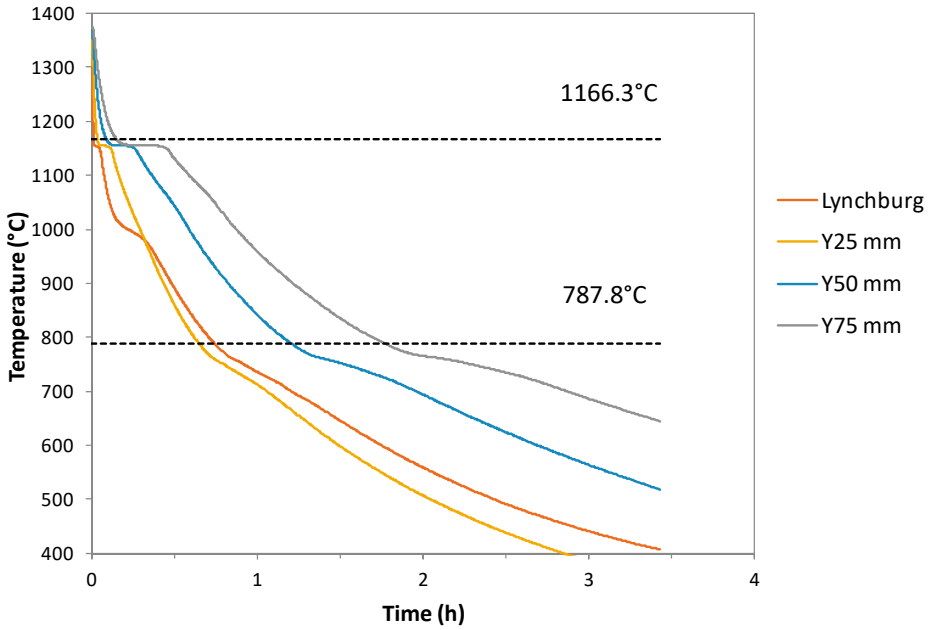

Figure 2. Simulations of temperature versus time of GJS 400 for the four different samples' geometry. The two dotted black lines represent eutectic and eutectoid equilibrium temperatures calculated through Equations (1) and (2), 1166.3 and 787.8 °C, respectively.

It can be seen (Figure 2 and Figure 4) that in the neighborhood of transformation temperatures the slope of the cooling curves varies abruptly because of the exothermic nature of eutectic and eutectoid transformation upon cooling. It can also be seen that for the Lynchburg sample at about 1000 °C the alloy experiences a reduction in cooling rate, which is an effect of the solidification occurring in the feeder.

As shown in Figure 3, indeed, the temperature decreases slower when the metal in the feeder undergoes solidification, an effect that disappears once solidification is complete. This phenomenon is not apparent in other molds because of their different geometries, and it is thought that it does not affect significantly microstructural features because it occurs far from the transformation temperatures.

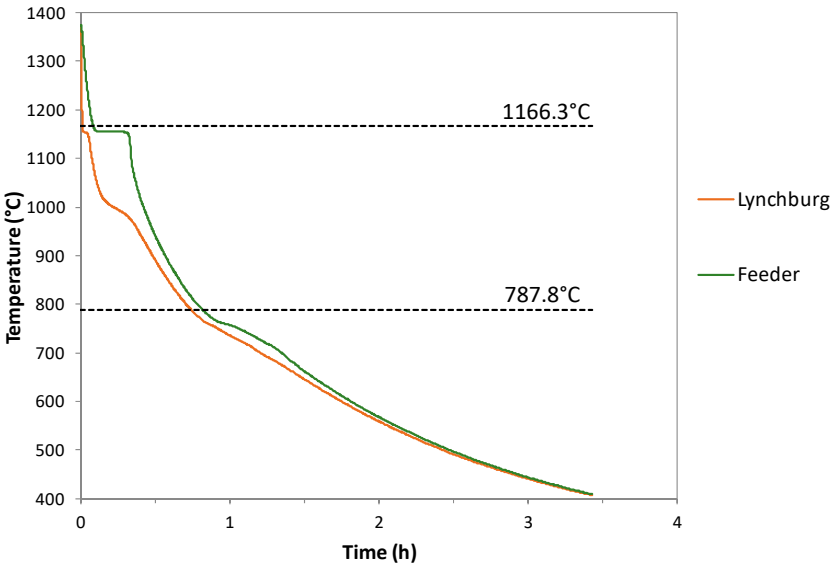

Figure 3. Simulations of temperature versus time of GJS 400 in different portions of the Lynchburg sample. When the alloy in the feeder undergoes solidification, cooling in the alloy in the lower portion is reduced. The two dotted black lines represent eutectic and eutectoid equilibrium temperatures calculated through Equations (1) and (2), 1166.3 and 787.8 °C, respectively.

Cooling rates near T_s and T_e (eutectic and eutectoid equilibrium temperatures, respectively) are given in Figure 4a,b, respectively. Table 2 summarizes cooling rates at the transformation temperatures, together with the undercooling experienced by the four samples, calculated as the difference between the eutectic temperature according to Equation (1) and the minimum temperature at the beginning of solidification.

Table 2. Undercooling at the eutectic transformation and cooling rate at transformation points for the four samples. Undercooling is calculated as the difference between the eutectic temperature according to Equation (1) and the minimum temperature at the beginning of solidification.

Mould	Undercooling (°C)	Cooling Rate at T_s [1] (°C/s)	Cooling Rate at T_e [2]
Lynchburg	11.56	1.98	0.09
Y25mm	11.39	0.56	0.11
Y50mm	10.45	0.16	0.06
Y75mm	9.96	0.10	0.04

[1] 1166.3 °C, according to Equation (1); [2] 787.8 °C, according to Equation (2).

Figure 4 and Table 2 show that the Lynchburg sample provided the fastest solidification rate, while at the eutectoid temperature the cooling rate is the second highest. It is worth noting that the differences in cooling rates are much higher at the eutectic temperature (there is a factor of about 20 between the highest and the lowest cooling rate), while at the eutectoid temperature they are comparable (only a factor of about 3). Moreover, variations in cooling rates are much higher in the

proximity of the eutectic temperature rather than around eutectoid temperature, as an effect of reduced heat transfer from metal to heated mold.

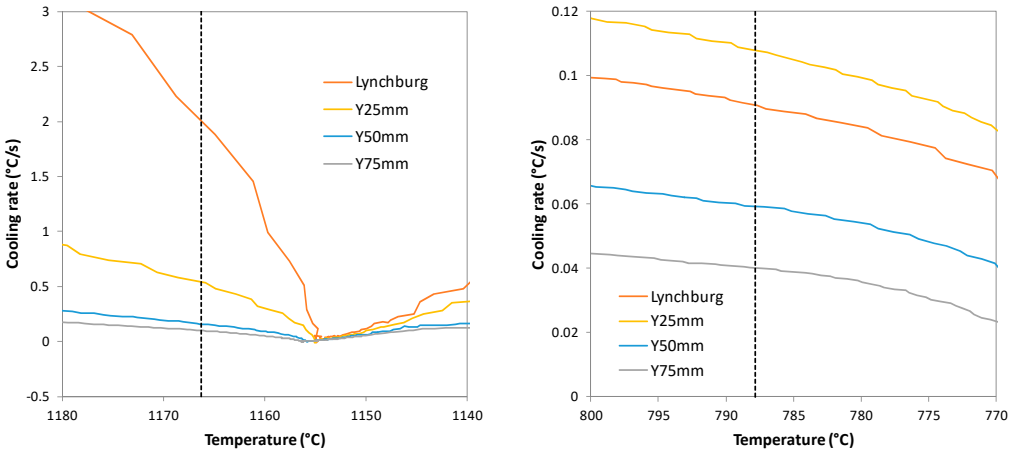

Figure 4. Cooling rate near to the equilibrium transformation temperatures calculated through Equations (1) and (2) for the four samples: (**a**) next to the eutectic temperature T_s, 1166.3 °C, calculated according to Equation (1) and indicated by the dotted black line (**b**) next to the eutectoid temperature T_e, 787.8 °C, calculated according to Equation (2) and indicated by the dotted black line. Steps are due to numerical derivation.

3.2. Microstructure

In Figure 5, representative SEM micrographs from Secondary Electron Imaging (SEI) of GJS 400 produced from the four different samples are reported. With slower solidification rates (Figure 4a) the microstructure became apparently coarser, with an evident increase of nodule size, while pearlite was present only in the specimens from Y-block samples (Figure 5b–d), and barely detectable in the specimens from Lynchburg sample (Figure 5a). This qualitative description can be supported through quantitative measurements according to ASTM standard E2567-16a [16]. Table 3 presents the results of image analysis, showing measurements on graphite features, defined in Section 2, and calculations on the volume fractions of the constituents. Together with the mean values, individual values measured on each specimen from each of the four samples are given.

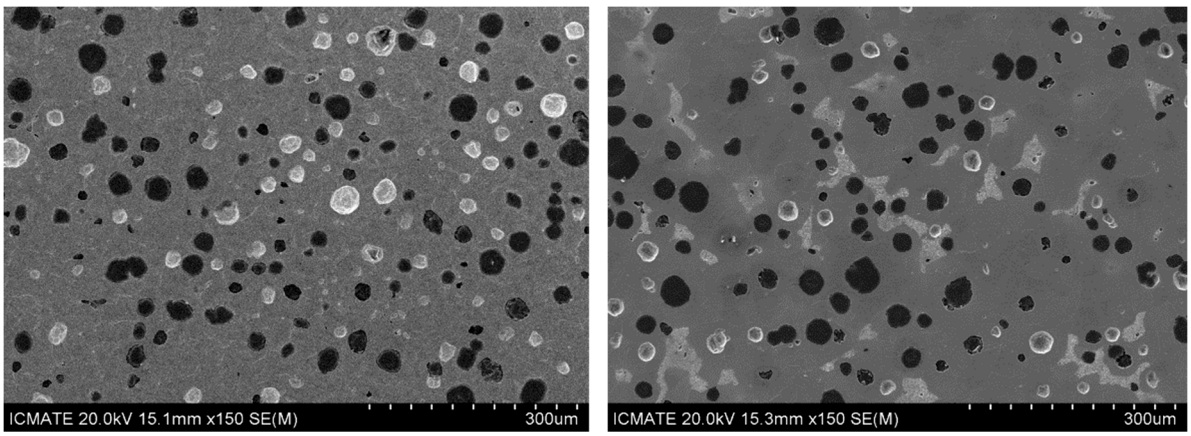

Figure 5. *Cont.*

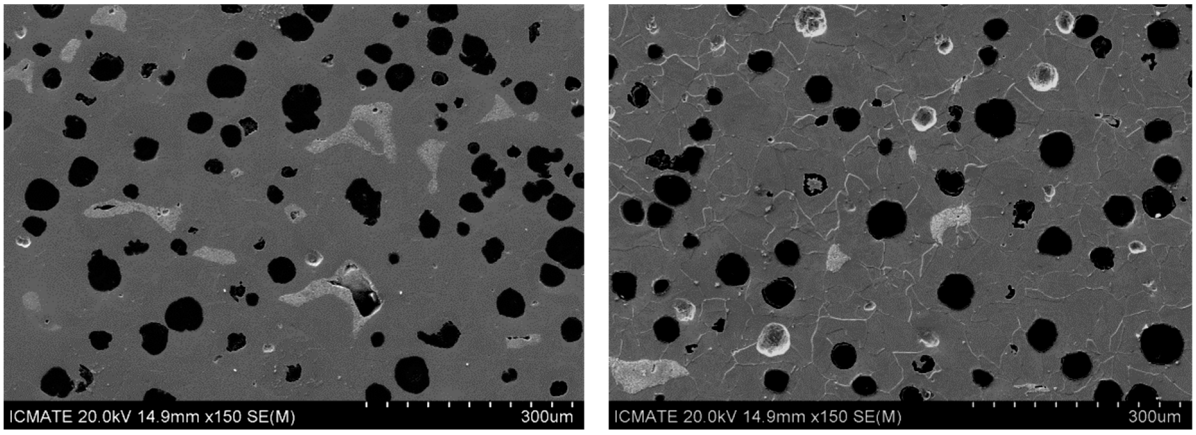

(**c**) (**d**)

Figure 5. SEM micrographs (SEI) of GJS 400 produced through four different samples; (**a**) Lynchburg; (**b**) Y 25 mm; (**c**) Y 50 mm; (**d**) Y 75 mm. Pearlitic islands are present only in Y-block samples.

Table 3. Image analysis results for the specimens from the four samples.

Sample	Specimen	Graphite Features			Volume Fractions			Ferrite Grain Size (μm)
		Nodule Count ($1/mm^2$)	Nodularity (%)	Mean Diameter (μm)	Graphite (%)	Ferrite (%)	Pearlite (%)	
Lynchburg	1	241	85.7	24.4	13.6	86.4	-	38.7
	2	256	86.5	23.9	13.2	86.7	-	34.2
	3	285	90.9	23.6	13.8	86.0	-	39.4
	4	254	92.1	25.2	14.0	85.8	-	40.8
	5	261	92.8	24.6	13.5	86.5	-	32.5
	6	268	90.8	24.1	13.5	86.2	-	38.0
	Mean	261 ± 15	89.8 ± 3.0	24.3 ± 0.6	13.6 ± 0.3	86.3 ± 0.4	-	37.3 ± 3.0
Y 25 mm	1	242	91.4	24.5	12.9	83.1	4.1	43.1
	2	233	92.5	25.4	13.1	83.0	3.9	38.9
	3	255	92.9	25.2	13.9	82.6	3.5	38.1
	4	227	88.9	24.2	11.8	85.0	3.2	40.4
	5	240	89.7	25.4	13.6	82.2	4.2	38.1
	6	253	91.5	24.4	12.9	83.0	4.1	36.7
	Mean	242 ± 11	91.2 ± 1.6	24.9 ± 0.5	13.0 ± 0.7	83.1 ± 1.0	3.9 ± 0.4	39.2 ± 2.3
Y 50 mm	1	139	88.8	30.6	11.9	84.9	3.2	50.3
	2	117	85.1	30.0	10.5	86.4	3.1	41.6
	3	95	85.8	32.6	10.0	84.4	5.6	46.2
	4	119	87.0	31.7	11.3	82.4	6.3	46.7
	5	116	88.4	32.0	11.0	85.9	3.1	54.0
	6	108	87.5	31.9	10.6	86.9	2.5	53.0
	Mean	116 ± 14	87.1 ± 1.4	31.5 ± 1.0	10.9 ± 0.7	85.1 ± 1.6	4.0 ± 1.6	48.6 ± 4.7
Y 75 mm	1	99	75.0	34.1	11.2	85.9	2.9	55.6
	2	97	85.8	34.6	11.6	85.1	3.3	53.7
	3	103	86.0	34.9	12.2	84.2	3.6	38.2
	4	98	87.3	34.7	11.3	85.5	3.2	40.8
	5	120	84.4	35.0	13.9	83.1	3.0	47.6
	6	110	80.9	33.6	12.3	85.6	2.1	50.3
	Mean	105 ± 9	83.2 ± 4.6	34.5 ± 0.5	12.1 ± 1.0	84.9 ± 1.1	3.0 ± 0.5	47.7 ± 7.0

In Figure 6a,b, SEM micrographs of a pearlite island in GJS 400 from Y 25 mm sample are reported. The clear lamellar pattern, i.e., parallel lamellae at an almost uniform distance, that can be seen in Figure 6b is not frequent, since pearlite often shows a complex configuration, in which the lamellar structure is irregular. Therefore, the characteristic widths of ferritic channels in the pearlitic islands could not be measured and can only be estimated to span between 100 and 300 nm, independently of cooling rates.

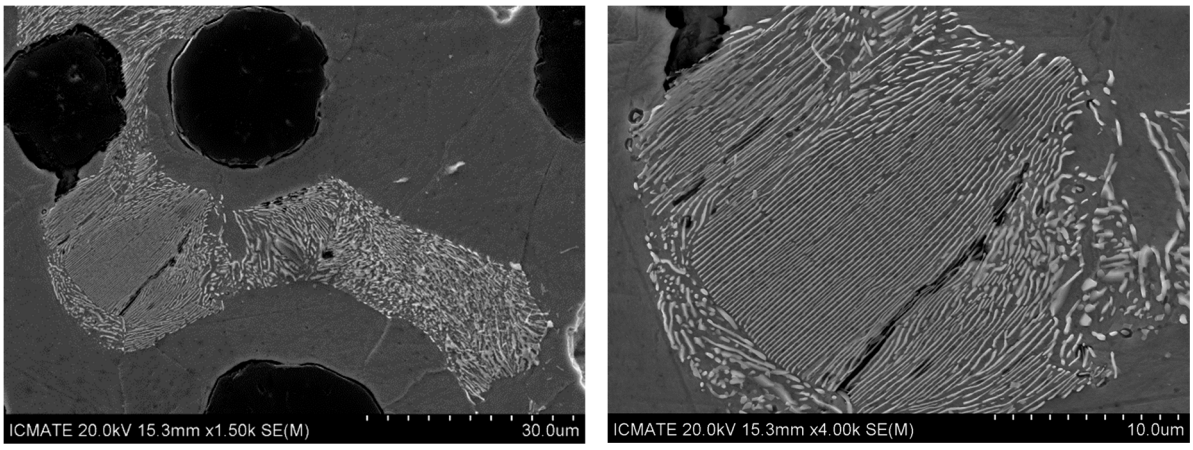

(**a**) (**b**)

Figure 6. SEM micrographs (SEI) of a typical pearlitic island in GJS 400 (Y 25 mm) with lamellar regions with ferritic channels of nanometric widths and irregular pearlite at different magnifications: (**a**) 1500 X; (**b**) 4000 X.

3.3. EDS Analyses

The local chemical composition of GJS 400 specimens from the four different samples was investigated through EDS. In particular, the concentration gradient of Si and Mn between couples of graphitic nodules was considered. Results are significantly different whether or not pearlite is present. Figure 7 shows a typical example of Si and Mn content in the region between two nodules separated by a pearlitic island (Y 75 mm sample). The Mn enrichment (positive segregation) and Si depletion (negative segregation) throughout pearlite is a common feature shown by every specimen, independently of the mold geometry. When there is no pearlite, neither Si nor Mn shows composition gradient (Figure 8).

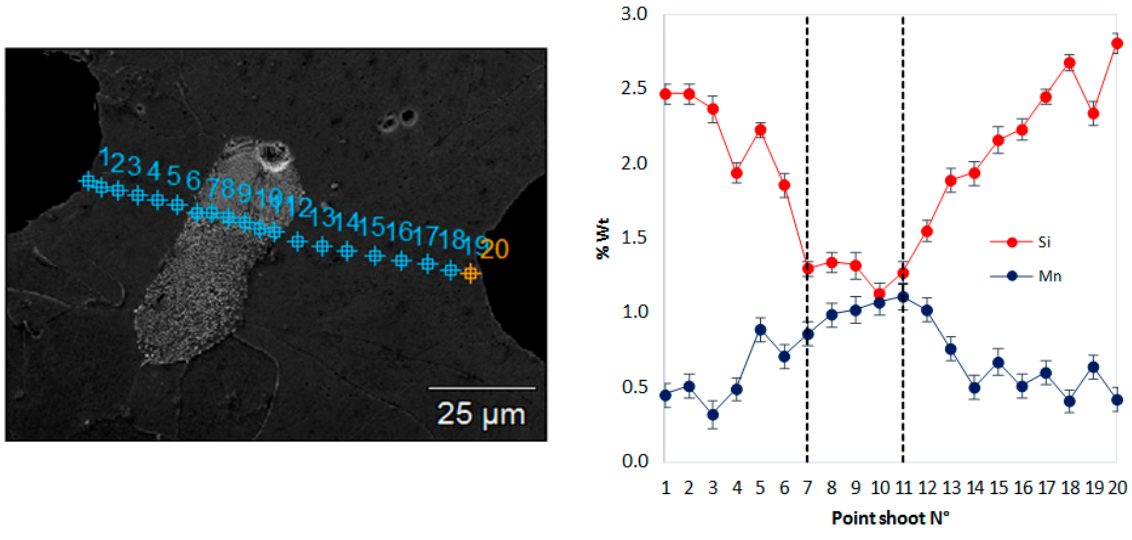

(**a**) (**b**)

Figure 7. Energy Dispersive X-ray Spectroscopy (EDS) investigation through a pearlitic island in GJS 400 (Y 75 mm sample): (**a**) EDS point shots positions; (**b**) gradients of Si and Mn compositions (wt.%) versus EDS point positions.

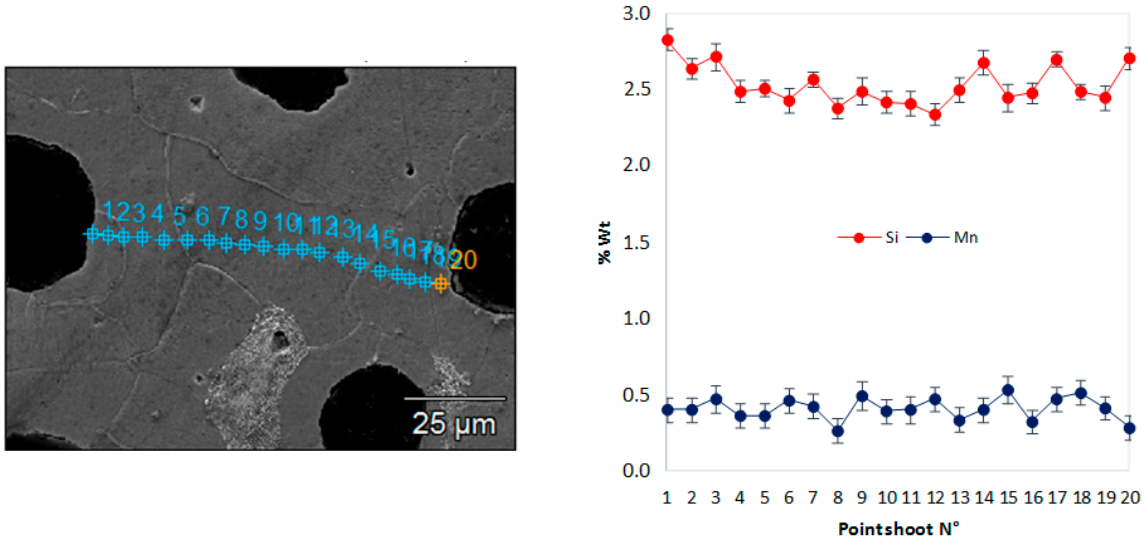

(**a**) (**b**)

Figure 8. EDS investigation through ferrite in GJS 400 (Y 75 mm sample): (**a**) EDS point shots positions; (**b**) gradients of Si and Mn compositions (wt.%) versus EDS point positions.

It has to be pointed out that the EDS probe overestimated the Mn content, which is about 0.1% (Table 1). This is thought to be an issue of EDS analysis itself, since it is difficult to determine the quantity of trace elements (concentration lower than about 1% wt). Mn content is indeed low and this could affect the absolute values given by the EDS measurements. Its gradient, though, can be considered significant.

4. Discussion

The GJS 400 microstructures are consistent with the simulated solidification rates (Figure 4), so that microstructural features result finer when cooling rates are higher (Table 3), in agreement with what reported in literature [10,31]. Nodule count measurement as a function of cooling rate at T_s (Figure 9) is consistent with the relationship found by Górny et al. in ductile iron with no Cu addition [10]. The presence of Cu in the alloys investigated in this work could account for the increase of nodule count at the same cooling rate.

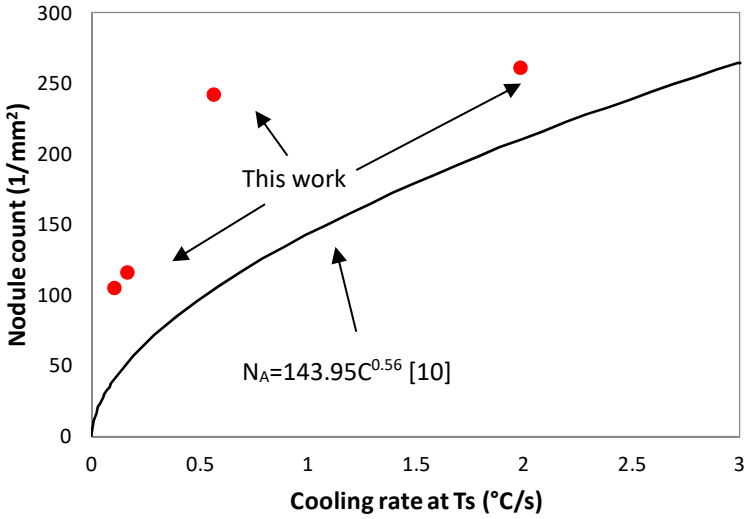

Figure 9. Nodule count (N_A) as a function of cooling rate (C) at the eutectic temperature T_s (red dots). The black line represents the relationship between cooling rate and nodule count in [10].

Higher cooling rates around eutectic temperature also lead to higher undercooling, which can be in turn fairly related to nodule count and nodule mean diameter (Figure 10).

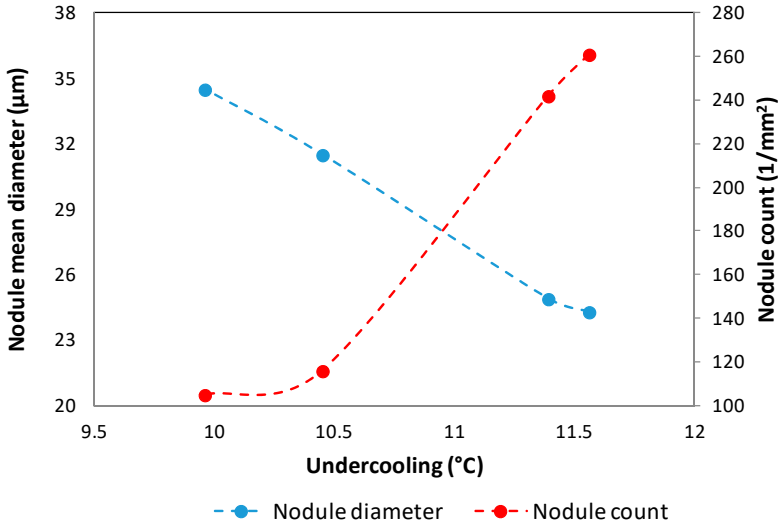

Figure 10. Nodule mean diameter and nodule count as functions of undercooling (difference between the eutectic temperature according to Equation (1) and the minimum temperature at the beginning of solidification).

Volume fraction of graphite, nodule count, and the mean nodule diameter, listed in Table 3, can be used to calculate the mean distance λ between graphite nodules through the Fullman's equation [32]:

$$\lambda = \frac{1 - V_g}{dN_A}, \tag{3}$$

where V_g is the volume fraction of graphite, N_A is the nodule count, and d is the mean diameter of the nodules.

The mean values for the four molds calculated through Equation (3) are reported in Table 4.

Table 4. Mean distance between graphitic nodules according to Equation (3).

Sample	Lynchburg	Y 25 mm	Y 50 mm	Y 75 mm
λ (µm)	136.2	144.4	243.8	242.7

The mean value for the Y 50 specimens is slightly higher than the one for the Y 75, despite the higher cooling rate, mainly because of the higher graphite volume fraction (Table 3).

The graphite content (Table 3, V_g in Equation (3)) is consistent with the Wojnar estimation [33] based on the carbon content of the alloy:

$$V_g = \frac{7.8\%C}{222 + 5.6\%C}. \tag{4}$$

Being %C the weight content of the alloy (3.63%), Equation (4) predicts a graphite volume fraction of 11.7%.

As already found in literature [20], ferritic grain size decreases when solidification rate increases (Figure 11).

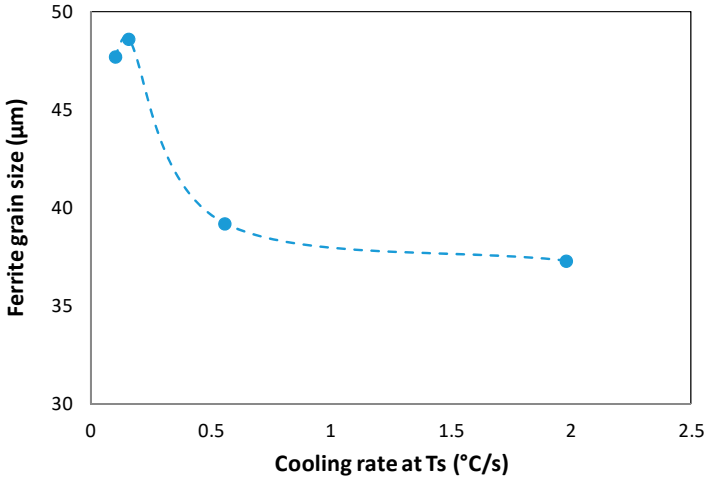

Figure 11. Ferrite grain size as a function of cooling rate at the eutectic temperature T_S.

While no apparent composition gradients can be seen in ferritic grains, pearlitic islands show positive Mn segregation and negative Si segregation (Figures 7 and 8), in agreement with literature [34–36]. These gradients are related to what happens during eutectic solidification. Mn is continuously rejected from the solidification front to the melt metal, making Mn content increase in the last to freeze zone, namely, the grain boundaries between nodules. Mn, as well as other carbide forming elements like Cr and V at the left side of Fe in the periodic table, promotes pearlite, which explains why it is found in pearlitic islands.

On the other hand, Si, which promotes graphite formation in the melt metal, tends to remain in the first to freeze zone, around the graphite nodules, promoting ferrite.

After solidification, solid state transformations take place. In particular, ferrite nucleates and grows in austenitic grains, which transforms into ferrite and graphite. If cooling is fast enough, thus allowing for larger undercooling, the eutectoid transformation occurs and pearlite forms [2,14].

Table 2 and Figure 4b show that cooling rates at the eutectoid temperature were low for all the four samples, and this is consistent with the very low pearlite volume fractions found. In the Lynchburg mold pearlite it is barely detectable, even if the cooling rate at the eutectoid transformation was higher than in Y 50 and Y 75 samples. This suggests that a major role was played by cooling rate at solidification which, at the eutectic temperature, was much higher in the Lynchburg mold. This may have reduced Mn segregations, thus lowering the pearlite content. So, pearlite may be the product of segregations during solidification rather than the result of different cooling rates through the intercritical interval Ar1-Ar3.

5. Conclusions

Different microstructures of GJS 400 were obtained through different geometries leading to different cooling rates, which were calculated through simulation of the actual gravity casting system. The microstructures were characterized in details, quantifying nodule count, nodularity, average diameter of the graphitic nodules, and volumetric fractions of graphite and pearlite compliant with the minimum requirements of statistics of the standard ASTM E2567-16a [28], and the average ferritic grain size complying with the standard ASTM E112-13 [29]. These features result finer as the solidification rate increases.

Positive segregation (enrichment) of Mn and negative segregation (depletion) of Si was observed in the pearlitic islands.

The cooling rates around the eutectoid temperature were very similar and very low, which prevented pearlite formation. Data suggest that the occurrence of pearlite is related to segregations during solidification, rather than to cooling rates at the eutectoid temperature.

This microstructural characterization provides the basis for the description and modeling of the tensile properties of GJS 400 alloy, the subject of a second part of this investigation [25].

Author Contributions: Conceptualization, G.A.; methodology, G.A.; software, S.M.; investigation, G.A., D.R., S.M.; resources, G.A., F.Z.; data analysis, G.A., D.R., S.M.; writing—original draft preparation, G.A.; writing—review and editing, D.R., M.G.; supervision, G.A.

Funding: This research received no external funding.

Acknowledgments: The authors would like to thank Davide Della Torre, Tullio Ranucci and Marcello Taloni for their experimental support.

Conflicts of Interest: The authors declare no conflict of interest.

References

1. Labrecque, C.; Gagné, M. Review Ductile Iron: Fifty Years of Continuous Development. *Can. Metall. Quart.* **1998**, *37*, 343–378. [CrossRef]
2. Tiedje, N.S. Solidification, Processing and Properties of Ductile Cast Iron. *Mater. Sci. Tech. Ser.* **2010**, *26*, 505–514. [CrossRef]
3. Fraś, E.; López, H. Eutectic Cells and Nodule Count—An Index of Molten Iron Quality. *Int. J. Metalcast.* **2010**, *4*, 35–61. [CrossRef]
4. Showman, R.E.; Aufderheide, R. A process for thin-wall sand castings. *AFS Trans.* **2003**, *111*, 567–578.
5. Juretzko, F.R.; Dix, L.P.; Ruxanda, R.; Stefanescu, D.M. Precondition of Ductile Iron Melts for Light Weight Casting: Effect on Mechanical Properties and Microstructure. *AFS Trans.* **2004**, *112*, 773–785.
6. Fraś, E.; López, H.; Podrzucki, C. The Influence of Oxygen on the Inoculation Process of Cast Iron. *Int. J. Cast Metal. Res.* **2000**, *13*, 107–121. [CrossRef]
7. Popescu, M.; Zavadil, R.; Thomson, J.; Sahoo, M. Studies to Improve Nucleation Potential of Ductile Iron When Using Carbidic Ductile Iron Returns. *AFS Trans.* **2007**, *115*, 591–608.
8. Fraś, E.; Górny, M. Fading of inoculation effects in ductile iron. *Arch. Foundry Eng.* **2008**, *8*, 83–88.
9. Fraś, E.; Górny, M.; López, H.F. Eutectic cell and Nodule Count in Cast Iron. Part I. Theoretical Background. *ISIJ Int.* **2007**, *47*, 259–268. [CrossRef]
10. Górny, M.; Tyrała, E. Effect of Cooling Rate on Microstructure and Mechanical Properties of Thin-Walled Ductile Iron Castings. *J. Mater. Eng. Perform.* **2013**, *22*, 300–305. [CrossRef]
11. White, D. Production of Ductile Iron Castings. In *ASM Handbook, Volume 1A: Cast Iron Science and Technology*; ASM International: Materials Park, OH, USA, 2017; pp. 603–611. [CrossRef]
12. Skaland, T.; Grong, O. Nodule Distribution in Ductile Cast Iron. *AFS Trans.* **1991**, *99*, 153–157.
13. Venugopalan, D. Prediction of Matrix Microstructure in Ductile Iron. *AFS Trans.* **1990**, *98*, 465–469.
14. Gerval, V.; Lacaze, J. Critical Temperature Range in Spheroidal Graphite Cast Irons. *ISIJ Int.* **2000**, *40*, 386–392. [CrossRef]
15. Górny, M.; Angella, G.; Tyrała, E.; Kawalec, M.; Paź, S.; Kmita, A. Role of Austenitization Temperature on Structure Homogeneity and Transformation Kinetics in Austempered Ductile Iron. *Met. Mater. Int.* **2019**, *25*, 956–965. [CrossRef]
16. Donnini, R.; Fabrizi, A.; Bonollo, F.; Zanardi, F.; Angella, G. Assessment of the microstructure evolution of an austempered ductile iron during austempering process through strain hardening analysis. *Met. Mater. Int.* **2017**, *23*, 855–864. [CrossRef]
17. Alhussein, A.; Risbet, M.; Bastien, A.; Chobaut, J.P.; Balloy, D.; Favergeon, J. Influence of silicon and addition elements on the mechanical behaviour of ferritic ductile cast iron. *Mater. Sci. Eng. A-Struct.* **2014**, *605*, 222–228. [CrossRef]
18. Lacaze, J.; Boudot, A.; Gerval, A.; Oquab, D.; Santos, H. The Role of Manganese and Copper in Eutectoid Transformation of Spheroidal Graphite Cast Iron. *Metall. Mater. Trans. A* **1997**, *28*, 2015–2025. [CrossRef]
19. Angella, G.; Zanardi, F.; Donnini, R. On the significance to use dislocation-density-related constitutive equations to correlate strain hardening with microstructure of metallic alloys: The case of conventional and austempered ductile irons. *J. Alloys Compd.* **2016**, *669*, 262–271. [CrossRef]
20. Hütter, G.; Zybell, L.; Kuna, M. Micromechanisms of fracture in nodular cast iron: From experimental findings 466 towards modeling strategies—A review. *Eng. Fract. Mech.* **2015**, *144*, 118–141. [CrossRef]

21. Goodrich, G.M. Cast iron microstructure anomalies and their causes. *AFS Trans.* **1997**, *105*, 669–683.
22. Iwabuchi, Y.; Narita, H.; Tsumura, O. Toughness and Ductility of heavy-walled ferritic spheroidal-graphite iron castings. *Res. Rep. Kushiro Natl. Coll.* **2003**, *37*, 1–9.
23. Nilsson, K.F.; Blagoeva, D.; Moretto, P. An experimental and numerical analysis to correlate variation in 472 ductility to defects and microstructure in ductile cast iron components. *Eng. Fract. Mech.* **2006**, *73*, 1133–1157. [CrossRef]
24. Nilsson, K.F.; Vokal, V. Analysis of ductile cast iron tensile tests to relate ductility variation to casting defects 475 and material microstructure. *Mater. Sci. Eng. A-Struct.* **2009**, *502*, 54–63. [CrossRef]
25. Angella, G.; Ripamonti, D.; Górny, M.; Masaggia, S.; Zanardi, F. The role of the microstructure on the tensile plastic behaviour of the ductile iron GJS 400 produced through different cooling rates. *Metals* **2019**, *9*, 1019. [CrossRef]
26. *EN 1563, Founding – Spheroidal Cast Irons*; European Committee for standardization (CEN): Brussels, Belgium, 2018.
27. ImageJ 1.51i. Available online: https://imagej.net (accessed on 30 March 2018).
28. *ASTM E2567-16a, Standard Test Method for Determining Nodularity and Nodule Count in Ductile Iron Using Image Analysis*; ASTM International: West Conshohocken, PA, USA, 2016. [CrossRef]
29. *ASTM E112-13, Standard Test Methods for Determining Average Grain Size*; ASTM International: West Conshohocken, PA, USA, 2013. [CrossRef]
30. Neuman, F. The influence of additional elements on the physic-chemical behaviour of carbon in saturated molten iron. In *Recent Research on Cast Iron*; Gordon and Breach: New York, NY, USA, 1998; pp. 659–705.
31. Rivera, G.; Boeri, R.; Sikora, J. Influence of the inoculation process, the chemical composition and the cooling rate, on the solidification macro and microstructure of ductile iron. *Int. J. Cast Metal. Res.* **2003**, *16*, 23–28. [CrossRef]
32. Fullman, R.L. Measurement of Particle Sizes in Opaque Bodies. *Trans. AIME* **1953**, *197*, 447–452. [CrossRef]
33. Wojnar, L.; Kurzydłowski, K.J.; Szala, J. Quantitative Image Analysis [for metallography]. In *Metallography and Microstructures*; ASM International: Materials Park, OH, USA, 2004; pp. 403–427.
34. Guo, X.; Stefanescu, D.M. Partitioning of alloying elements during the eutectoid transformation of ductile iron. *Int. J. Cast Metal. Res.* **1999**, *11*, 437–441. [CrossRef]
35. Boeri, R.; Weinberg, F. Microsegregation of Alloying Elements in Cast Iron. *Int. J. Cast Metal. Res.* **1993**, *6*, 153–158. [CrossRef]
36. Chiniforush, E.A.; Iranipour, N.; Yazdani, S. Effect of nodule count and austempering heat treatment on segregation behavior of alloying elements in ductile cast iron. *China Foundry* **2016**, *13*, 217–222. [CrossRef]